

Photon Anti-Bunching and Quantum Non-Gaussianity from High-Harmonic Generation

David Theidel^{1,*}, Mackrine Nahra¹, Ilya Karuseichyk¹, Houssna Griguer¹, Mateusz Weis¹, and Hamed Merdji¹

¹*Laboratoire d'Optique Appliquée (LOA), CNRS, École polytechnique, ENSTA, Institut Polytechnique de Paris, Palaiseau, France*

Quantum technologies are powered by platforms to generate complex non-classical states of matter or light to realize applications. We investigate the non-classical properties of high-harmonic generation in semiconductors, an emerging photonic platform. Measuring the click statistics of three double-digit orders, we evaluate witness operators to certify the non-classicality of the generated states. We show that higher-order harmonics driven by a coherent laser are squeezed and entangled. The properties of the emission are well retrieved with an entangled Gaussian state model, obtained by numerical state optimization to multiple observables. Additionally, we perform inter-order heralded measurements to engineer the quantum state of the emission. The heralded states have distinct properties, showing anti-bunched photon statistics. Further, we witness the generation of a quantum non-Gaussian state, a resource highly relevant for quantum information. With this, we establish high-harmonic generation as a platform for generating quantum optical resources.

Introduction - High-Harmonic Generation (HHG) is a unique effect in physics that led to advancements in our understanding of matter, light and fundamental particles like electrons [1–6].

Generally, the generation of non-classical light is mediated by non-linear interactions in atoms or engineered crystals. The process of HHG is in itself highly non-linear, raising questions about the nature of the generated state of light. Recently, theoretical and experimental efforts have opened a new perspective, bridging the fields of quantum optics and strong-field physics [7–17]. These works address several open questions, including the presence and origin of non-classical effects in emitted light, as well as the influence of non-classical driving beams and correlated materials on HHG. In this line of research, semiconductor HHG (SHHG) has a unique place. Even with a coherent driving laser, the interaction in semiconductors is suggested to result in intrinsic non-classical properties in the radiation [11, 14, 18–20]. This is in contrast to approaches adding a perturbation in the driving light with a bright-squeezed vacuum state [10, 12, 16, 21].

In this work, we extend these studies to double-digit high-harmonic orders. We certify the non-classicality of the generated states by evaluating criteria based on the photon counting statistics. The statistics of the state are obtained with single-photon detection. Using numerical optimization including multiple non-classical observables, we find an effective state with properties that reproduce our experimental data.

Further, we demonstrate for the first time quantum state engineering on the harmonics. Performing conditional measurements between two spectrally distinct harmonic orders, we generate a heralded state with distinct properties. We show that the heralded state exhibits anti-bunching, a hallmark witness for non-classicality. More intriguingly, we evaluate a witness operator and confirm the measurement-induced generation of a quantum non-Gaussian state. Quantum non-Gaussian states are essential resources for universal quantum computation with continuous variables and for quantum error correction protocols [22–27].

Quantifying non-classicality via photon statistics -

The experimental scheme is schematically depicted in Fig. 1a). Ultrashort laser pulses, with a central wavelength of 7.7 μm, generated at a repetition rate of 330 kHz, are focused on a semiconductor crystal (CdTe[110]). In a strong-field interaction, higher-order harmonics are generated at integer multiples of the driving laser frequency [28–30]. Figure 1b) shows the measured SHHG spectrum. The higher-order harmonics are clearly visible from the 8th to the 15th order. Using spectral filters and beam splitters, we select and spatially separate three orders (H11, H12, H13) for the detection. Single-photon avalanche photodiodes are arranged in a Hanbury-Brown and Twiss geometry. This enables the detection of single-photon events as well as coincidence events (simultaneous photon arrivals) resolved by their relative arrival time τ . The coincidence events are measured as auto- and cross-correlations histograms inside one spectral order and between distinct orders. The coincidence detection window is set to 100 ns, much less than the duration between two subsequent excitation pulses. Additionally, one detector is employed as a herald, to condition the measurements of the other detectors on a successful detection.

First, we will discuss the result for the unheralded detection of photon counting statistics. Normalizing the time-resolved histogram of photon arrival times, we can calculate the intensity correlation function

$$g_{H(i,j)}^{(2)} = \frac{\langle \hat{a}_i^\dagger \hat{a}_j^\dagger \hat{a}_i \hat{a}_j \rangle}{\langle \hat{a}_i^\dagger \hat{a}_i \rangle \langle \hat{a}_j^\dagger \hat{a}_j \rangle} \quad (1)$$

at $\tau = 0$ for a single harmonic order ($i = j$) or between two spectrally distinct orders ($i \neq j$). Here, \hat{a}_i^\dagger and \hat{a}_i denote the creation and annihilation operators for a photon attributed to harmonic order i . The value of the intensity correlation function depends on the photon number statistics of the detected state. The intensity correlation function quantifies the similarity of the photon number distribution to the Poissonian distribution of a coherent state, based on the first two moments. If the variance of the photon number distribution is greater than the mean, photons tend to arrive

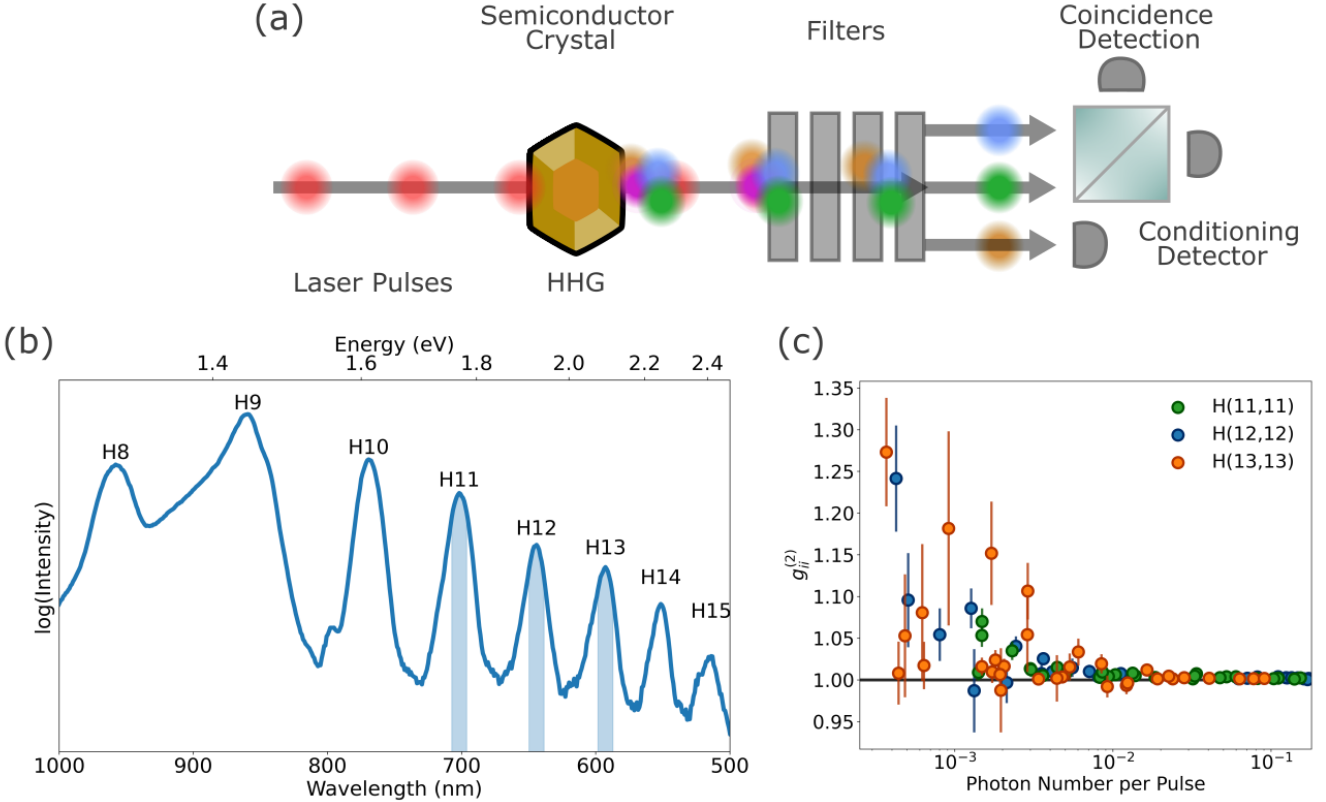


Figure 1. Schematic of the experimental setup and properties of the emitted radiation. (a) Ultrashort laser pulses in the infrared spectral range interact with the electrons inside a semiconductor crystal. During the interaction, higher-order harmonics are generated as a frequency comb. After selecting three orders with spectral filters, single-photon detection is performed to acquire the mean number of photons as well as the number of simultaneous photon detection events between the detectors. One detector is used as a herald, to condition the measurement of the other detectors on successful detection of a herald photon. (b) From the HHG spectrum three orders (H_{11} , H_{12} , H_{13}) are selected for analysis. The intensity is shown in logarithmic scaling. The colored region indicates the spectral width of the employed filters. (c) Measured normalized intensity correlation function $g_{H(i,i)}^{(2)}$ calculated from single- and coincidence events produced from photons of single harmonic order ($i = j$). At low mean photon numbers, photon bunching is observed.

in bunches, if the variance is smaller, the photon arrival times are anti-bunched. Here, a value $g^{(2)}(0) = g^{(2)} = 1$ indicates no photon bunching, $g^{(2)}(0) > g^{(2)}(\tau)$ bunched and $g^{(2)}(0) < g^{(2)}(\tau)$ anti-bunched light. As only non-classical states exhibit $g^{(2)}(0) < g^{(2)}(\tau)$, the intensity correlation function is a useful non-classicality witness [31, 32]. In contrast, $g^{(2)}(0) = 1$ is always obtained for a coherent state.

We sweep the driving laser intensity to control the mean number of photons $\langle \hat{n}_i \rangle = \langle \hat{a}_i^\dagger \hat{a}_i \rangle$ and measure $g_{H(i,i)}^{(2)}$. The results for the auto-correlations are shown in Figure 1c). The error bars are calculated assuming Poissonian error statistics and error propagation. We observe $g_{H(i,i)}^{(2)} > 1$ at the lowest intensity, indicating photon bunching from super-Poissonian number statistics. At higher driving laser intensities and detector count rates, $g_{H(i,i)}^{(2)} = 1$ for all harmonic orders. This trend is similar to previous reported values on low-order harmonics [11, 14]. Although the photon bunching is not as prominent as for the lower-order harmonics, a significant deviation from the coherent state statistics is observed.

The reduced bunching at higher orders can be at-

tributed to the difference in the generation mechanism. In semiconductors, the process is often conceptually split into two main contributions, namely intraband and interband harmonics. Intraband harmonics are generated from Bloch electrons oscillating inside a single band, while interband harmonics are generated via recombination of electron-hole pairs [30]. For low-order harmonics generated with mid-infrared pulses interband currents and perturbative, multi-photon excitation dominate the emission. Additionally, re-excitation effects at high repetition rates may enhance interband contributions and lead to electronic correlation between the currents. Higher-orders from far-infrared pulses are generated mainly as intraband harmonics [33]. In general, when the pump intensity is increased, the relative contribution of interband harmonics drops. This possibly explains the scaling of the intensity correlation function, in addition to multimodal detection effects [14]. Theoretical treatments suggest non-classicality emerging from both processes, although the microscopic origin of non-classicality is still the subject of current research [15, 18–20, 34].

Evaluation of Non-Classicality Criteria - In the case

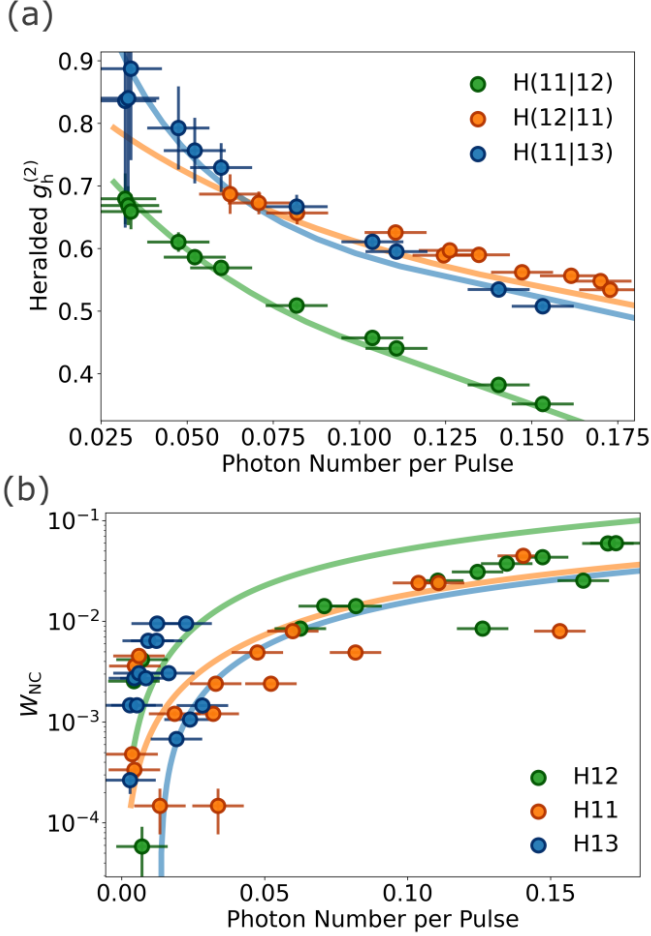


Figure 2. Non-Classicality Criteria. (a) The heralded intensity correlation function $g_{H(i|j)}^{(2)}$ of the state is shown over the mean photon number of harmonic i . Single detection events on the herald harmonic j are used to condition the detection of simultaneous events on the signal harmonic order i . The heralded states have distinct photon statistics, showing anti-bunching with $g_h^{(2)} < 1$. (b) Based on the photon detection probabilities a non-classicality witness can be derived. For all harmonics (H11, H12, H13) $W_{NC} > 0$ certifies that the unheralded, initial harmonic state cannot be expressed as a mixture of coherent states.

of a low number of mean photons, complementary non-classicality criteria can be analysed. A state is non-classical if it cannot be expressed as a mixture of coherent states [35]. To test this, we evaluate the inequality

$$W_{NC} = P_S - 2(\sqrt{P_C} - P_C) > 0 \quad (2)$$

where P_S and P_C are respectively the measured probabilities for a single detection event and simultaneous coincidence event [36]. We name the quantity on the left of Eq. (2) W_{NC} the non-classicality witness. The probabilities P_S and P_C can be directly obtained from the recorded single event- and simultaneous event rates. The results are shown in Figure 2b) for a single harmonic order and in Figure S2 for the cross-correlation between two different harmonic orders. In both cases, positive values ($W_{NC} > 0$) indicate that the state is non-classical. We observe a trend, where the violation increases and

then flattens. The trendlines in the plots are the result of our generalized Gaussian state model, discussed in more detail below.

Next, we explore a conditional measurement protocol, with the goal of generating states with distinct properties. Practically, performing conditioning means realizing a detection operation dependent on the success of a second event. This allows for implementing non-deterministic single-photon sources [37, 38]. When a photon pair source emits two single-photons into distinct modes, the detection of a photon in one mode heralds the presence of a photon in the second.

We condition the measurement of a photon of e.g. harmonic 11 (signal) on a photon detection event at harmonic 13 (herald). We label this heralded state as $H(11|13)$. We apply this method to our measurement platform comprising three SHHG orders denoted as H11, H12 and H13.

We set our measurement to a low mean number of photons $\langle \hat{n} \rangle < 0.2$ in the detection arms, so that the probability for a three-photon emission is effectively zero $\langle 3|\rho|3 \rangle \approx 0$. We therefore approximate the measured state as $\hat{\rho} \approx p_0|0\rangle\langle 0| + p_1|1\rangle\langle 1| + p_{2+}|2\rangle\langle 2|$, with the vacuum probability p_0 , the single-photon probability p_1 and the probability for a 'two-or-more' photon event $p_{2+} = 1 - p_0 - p_1$. In this approximation, the heralded intensity correlation function is

$$g_h^{(2)}(0) = \frac{2p_{2+}}{p_1^2} = \frac{2(1 - p_0 - p_1)}{(2(1 - p_0) - p_1)^2}. \quad (3)$$

We calculate the probabilities from the acquired count rates [39–44]. Similar to before, error bars for $g_h^{(2)}$ are calculated by error propagation assuming Poissonian error statistics. The error in the photon number stems from fluctuations in laser intensity during long measurements. For all combinations, we observe anti-bunching with $g_h^{(2)} < 1$ (Fig. 2a)), demonstrating that the heralded states are non-classical. The magnitude of anti-bunching is comparable to early demonstration of multiplexed single-photon sources [45–47]. We observe an opposite trend to what is usually reported for photon pairs based on parametric sources [48, 49]. Indeed, the anti-bunching gets stronger with an increase in the mean photon number. We explain this scaling with high vacuum contributions p_0 and low single-photon detection probabilities p_1 at low driving laser intensities, as retrieved by our numerical model.

Quantum Non-Gaussian Witness - Of high interest are a subset of non-classical states, called quantum non-Gaussian (QNG) states [25]. A state is quantum non-Gaussian if it cannot be expressed as a convex mixture of Gaussian states, meaning $\rho \notin \mathcal{G}$, where \mathcal{G} is the set of Gaussian states [50].

Analogous to a non-classicality or entanglement witness, a QNG witness is an operator that certifies whether the measured state $\rho \notin \mathcal{G}$. We evaluate such an operator entirely relying on the probabilities for vacuum, single-photon and multi-photon events [26]. The witness is based on the definition of a linear function

$$W(a) = ap_0 + p_1 \quad (4)$$

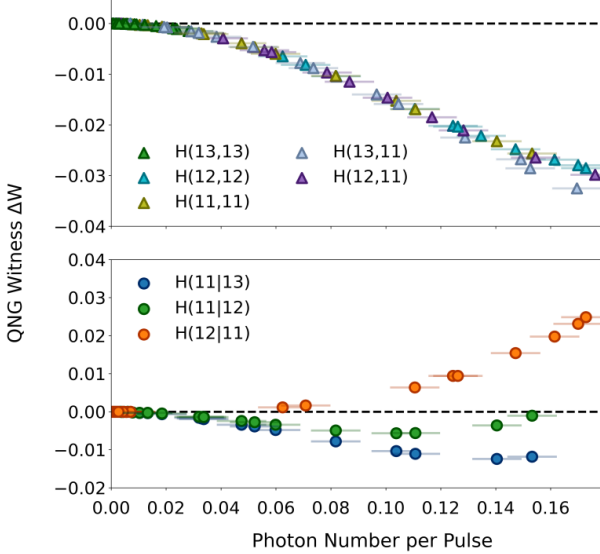


Figure 3. Quantum non-Gaussian Witness. The witness violation strength $\Delta W = W(a) - W_G(a)$ is plotted as a function of signal count rate for the initial (top) and heralded (bottom) states across over the mean photon number. Data points above the dashed zero line with $\Delta W > 0$ certify the quantum non-Gaussian nature of the measured states.

where a is a free parameter, $p_0 = \langle 0 | \rho | 0 \rangle$ is the vacuum probability and $p_1 = \langle 1 | \rho | 1 \rangle$ is the single-photon probability, estimated from the measured statistics. A state is certified QNG, $\rho \notin \mathcal{G}$, if $W(a) > W_G(a)$, where $W_G(a) = \max_{\rho \in \mathcal{G}} W(a)$ is the maximum value achieved by any Gaussian state. The boundary is computed from the Gaussian state probabilities

$$p_0 = \frac{e^{-d^2[1-\tanh(r)]}}{\cosh(r)}, \quad (5)$$

$$p_1 = \frac{d^2 e^{-d^2[1-\tanh(r)]}}{\cosh^3(r)} \quad (6)$$

with r the squeezing parameter and the displacement given as $d^2 = (e^{4r} - 1)/4$. For each value of a , we numerically maximize $W(a)$ over r using these expressions to obtain $W_G(a)$ [36, 40]. The witness violation strength is quantified by

$$\Delta W = W(a) - W_G(a) \quad (7)$$

where subsequent maximization over the free parameter a identifies the optimal witness for the measured state. If $\Delta W > 0$, the state is QNG.

The top plot in Fig. 3 shows the witness strength evaluated for the initial harmonic states. As expected, the witness is not fulfilled. For the heralded states, we find that the combination $H(12|11)$ is certified QNG (Fig. 3 bottom). In total, eleven datapoints significantly cross the dedicated bound. The other two combinations show an encouraging trend, but do not cross the necessary bound in the presented region. This is likely caused by the higher heralding efficiency on the intense eleventh harmonic, leading to better signal-to-noise ratio on the heralded state. We note, that in our ex-

perimental scheme, the generation of a quantum non-Gaussian state is measurement induced, caused by the conditional, non-Gaussian operation on the unheralded quantum state [25, 37].

The certification of a QNG state leads us to more insights about the nature of non-classical correlations between the harmonic orders. Current experiments and theoretical works suggest that the initial, unheralded state is a Gaussian state [7, 11, 14, 18]. In this case, entanglement between the harmonic orders is a required resource, to generate a heralded QNG state [25]. This follows because conditional operations on separable Gaussian states always yield states expressible as convex mixtures of Gaussians.

Numerical Model - To solidify our interpretation of our experimental data, we perform a constrained state reconstruction. We aim to find an effective state reproducing the main trends and non-classicality features. The effective model is based on a generalized two-mode Gaussian state, constructed by first taking a product of two thermal states and then applying a sequence of beam-splitter, squeezing, and displacement operations. The heralded state is obtained by projection onto successful detection. The state is parametrized and optimized against the non-classical observables [39]. The quantum non-Gaussian depth, an additional metric for QNG robustness is used for the optimization and is discussed in the Supplementary Material [39, 51].

We jointly depict the experimental data and the scaling retrieved from the respective optimized, effective state in Fig. 2 and Fig. S2. The simultaneous convergence of the model across five independent observables provides strong evidence for the underlying entangled nature of the state, despite the large parameter space.

Analysing the states properties, we find that all states exhibit single-mode squeezing and displacement (Fig. 4a) and b). Initially, the squeezing and displacement are weak, supporting the interpretation of the scaling of $g_h^{(2)}$ due to vacuum contributions. Both contributions increase with a higher mean photon number of the state.

The magnitude of squeezing depends on the role of the harmonic, being used for conditioning or not. In general, the squeezing is higher in the signal mode. The asymmetry of bipartite reduction hints at a complex global state structure. This is already indicated by the difference in harmonic intensities implying that the state formed by modes with different photon numbers. This is in contrast to the frequently analysed two-mode squeezed vacuum states. It is an important insight for future works, as most studies and theoretical treatments focus on the properties of symmetric states.

Most importantly, to model the data adequately it is necessary that the two harmonic orders are entangled. This is quantified by the logarithmic negativity $E_N(\rho) = \log_2(\|\rho_{AB}^{T_B}\|_1)$, where T_B denotes the partial transpose with respect to mode B [52, 53]. Our numerically retrieved state is certified entangled as $E_N(\rho) > 0$ for all combinations (Fig. 4c). Still, the state is highly mixed. Therefore, it is not steerable due to contribution of classical thermal noise and displacement [54].

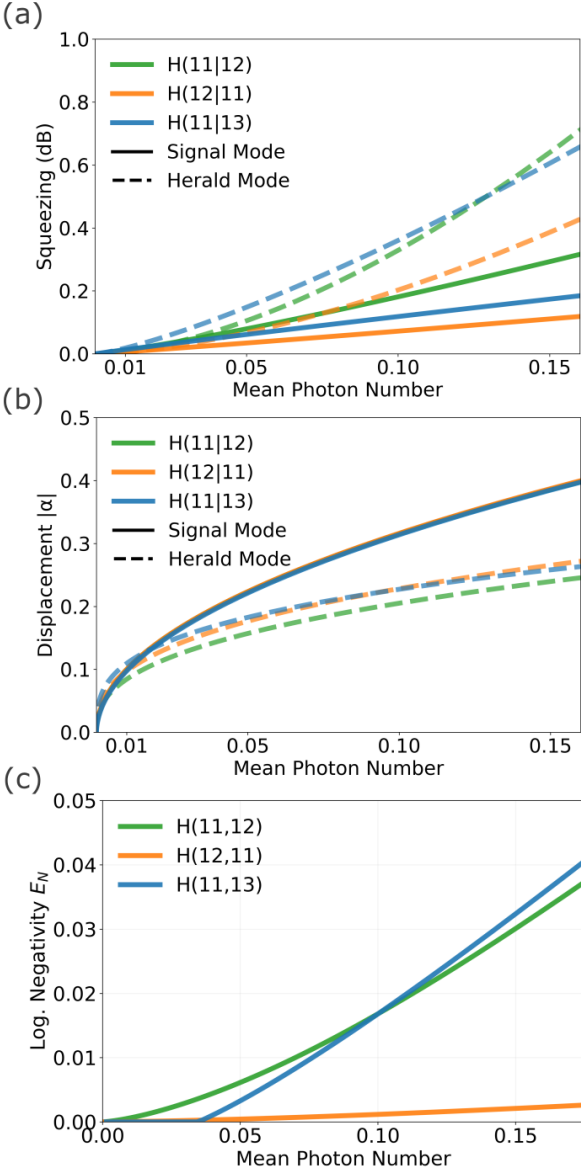


Figure 4. Properties of the effective state. The modelled state is found by optimizing a generalized two-mode Gaussian state to the experimentally recorded non-classicality observables. We depict the properties of the reduced states. For $H(i|j)$, the harmonic order j takes the role of the herald, to conditionally create the heralded state in harmonic order i . The modelled states show squeezing (a) and displacement, scaling with the mean photon number. The initial unheralded states $H(i,j)$ are entangled as quantified by the non-zero logarithmic negativity c).

Concluding, our experimental data and numerical model is compatible with an initial, non-classical Gaussian state. Focusing on two harmonic orders, we perform inter-harmonic heralding and convert the state into a distinct non-classical state exhibiting photon anti-bunching. In one case, the QNG nature of the heralded state is certified. This result, as well as our numerical model, suggest that the two harmonic orders used in the conditional measurement scheme, are entangled.

SUMMARY AND OUTLOOK

In this work, we make significant steps in establishing SHHG as a source of non-classical states. We evaluate non-classicality witnesses based on the photon counting statistics and confirm the presence of non-classical features in high-order harmonics generated in CdTe. This confirms and extends previous results of the intrinsic non-classicality of SHHG to double-digit harmonics generated with a distinct laser system. Further, by heralding the SHHG state, we observe photon anti-bunching $g^{(2)} < 1$. Extending the analysis to a QNG witness, we certify the creation of a QNG state. Our results and effective state model suggest that the underlying quantum state itself is non-classical and likely entangled. As a prospect, the SHHG source can be analysed in more complex schemes including the measurement of an entanglement witness and the inclusion of additional spectral orders. Then, using a high number of modes, the harmonics could be employed as ancillary modes for non-deterministic single-photon generation for further manipulation [23, 27, 55].

* david.theidel@polytechnique.edu

- [1] M. Ferray, A. L'Huillier, X. F. Li, L. A. Lompre, G. Mainfray, and C. Manus, Journal of Physics B: Atomic, Molecular and Optical Physics **21**, L31 (1988).
- [2] M. Lewenstein, P. Balcou, M. Y. Ivanov, A. L'huillier, and P. B. Corkum, Physical Review A **49**, 2117 (1994).
- [3] P.-M. Paul, E. S. Toma, P. Breger, G. Mullot, F. Augé, P. Balcou, H. G. Muller, and P. Agostini, Science **292**, 1689 (2001).
- [4] M. Hentschel, R. Kienberger, C. Spielmann, G. A. Reid, N. Milosevic, T. Brabec, P. Corkum, U. Heinzmann, M. Drescher, and F. Krausz, Nature **414**, 509 (2001).
- [5] P. Agostini and L. F. DiMauro, Reports on progress in physics **67**, 813 (2004).
- [6] P. B. Corkum and F. Krausz, Nature physics **3**, 381 (2007).
- [7] A. Gorlach, O. Neufeld, N. Rivera, O. Cohen, and I. Kaminer, Nature Communications **11**, 4598 (2020).
- [8] Á. Gombkötő, S. Varró, P. Mati, and P. Földi, Physical Review A **101**, 013418 (2020).
- [9] A. Pizzi, A. Gorlach, N. Rivera, A. Nunnenkamp, and I. Kaminer, Nature Physics **19**, 551 (2023).
- [10] A. Gorlach, M. E. Tzur, M. Birk, M. Krüger, N. Rivera, O. Cohen, and I. Kaminer, Nature Physics **19**, 1689 (2023).
- [11] D. Theidel, V. Cotte, R. Sondenheimer, V. Shiriaeva, M. Froidevaux, V. Severin, A. Merdji-Larue, P. Mosel, S. Froehlich, K.-A. Weber, *et al.*, PRX Quantum **5**, 040319 (2024).
- [12] A. Rasputnyi, Z. Chen, M. Birk, O. Cohen, I. Kaminer, M. Krüger, D. Seletskiy, M. Chekhova, and F. Tani, Nature Physics **20**, 1960 (2024).
- [13] P. Stammer, J. Rivera-Dean, A. S. Maxwell, T. Lamprou, J. Argüello-Luengo, P. Tzallas, M. F. Ciappina, and M. Lewenstein, Physical review letters **132**, 143603 (2024).
- [14] D. Theidel, V. Cotte, P. Heinzel, H. Griguer, M. Weis, R. Sondenheimer, and H. Merdji, Physical Review Research **7**, 033223 (2025).

- [15] S. Yi, N. D. Klimkin, G. G. Brown, O. Smirnova, S. Patchkovskii, I. Babushkin, and M. Ivanov, *Physical Review X* **15**, 011023 (2025).
- [16] S. Lemieux, S. A. Jalil, D. N. Purschke, N. Boroumand, T. Hammond, D. Villeneuve, A. Naumov, T. Brabec, and G. Vampa, *Nature Photonics* , 1 (2025).
- [17] C. S. Lange and L. B. Madsen, *Physical Review A* **111**, 013113 (2025).
- [18] I. Gonoskov, R. Sondenheimer, C. Hünecke, D. Kortashov, U. Peschel, and S. Gräfe, *Physical Review B* **109**, 125110 (2024).
- [19] J. Rivera-Dean, P. Stammer, A. S. Maxwell, T. Lamprou, A. F. Ordóñez, E. Pisanty, P. Tzallas, M. Lewenstein, and M. F. Ciappina, *Physical Review B* **109**, 035203 (2024).
- [20] J. Li, Z. Lyu, H. Liu, and Y. Liu, *Physical Review A* **112**, 033507 (2025).
- [21] M. E. Tzur, M. Birk, A. Gorlach, I. Kaminer, M. Krüger, and O. Cohen, *Physical Review Research* **6**, 033079 (2024).
- [22] A. Mari and J. Eisert, *Physical review letters* **109**, 230503 (2012).
- [23] U. L. Andersen, J. S. Neergaard-Nielsen, P. Van Loock, and A. Furusawa, *Nature Physics* **11**, 713 (2015).
- [24] A. I. Lvovsky, P. Grangier, A. Ourjoumtsev, V. Parigi, M. Sasaki, and R. Tualle-Brouri, *arXiv preprint arXiv:2006.16985* (2020).
- [25] M. Walschaers, *PRX Quantum* **2** (2021).
- [26] L. Lachman and R. Filip, *Progress in Quantum Electronics* **83**, 100395 (2022).
- [27] H. Wang, T. C. Ralph, J. J. Renema, C.-Y. Lu, and J.-W. Pan, *Nature Materials* **24**, 1883 (2025).
- [28] S. Ghimire, A. D. DiChiara, E. Sistrunk, P. Agostini, L. F. DiMauro, and D. A. Reis, *Nature physics* **7**, 138 (2011).
- [29] S. Ghimire and D. A. Reis, *Nature physics* **15**, 10 (2019).
- [30] L. Yue and M. B. Gaarde, *Journal of the Optical Society of America B* **39**, 535 (2022).
- [31] R. Loudon, *Reports on progress in physics* **43**, 913 (1980).
- [32] P. Grangier, G. Roger, and A. Aspect, *Europhysics Letters* **1**, 173 (1986).
- [33] Z. Wang, H. Park, Y. H. Lai, J. Xu, C. I. Blaga, F. Yang, P. Agostini, and L. F. DiMauro, *Nature communications* **8**, 1 (2017).
- [34] C. S. Lange, T. Hansen, and L. B. Madsen, *Physical Review A* **109**, 033110 (2024).
- [35] R. J. Glauber, *Physical Review* **131**, 2766 (1963).
- [36] L. Lachman and R. Filip, *Physical Review A* **88**, 063841 (2013).
- [37] A. I. Lvovsky, H. Hansen, T. Aichele, O. Benson, J. Mlynek, and S. Schiller, *Physical Review Letters* **87**, 050402 (2001).
- [38] P. Senellart, G. Solomon, and A. White, *Nature nanotechnology* **12**, 1026 (2017).
- [39] Supplementary information, URL_will_be_inserted_by_publisher (2026).
- [40] M. Ježek, I. Straka, M. Mičuda, M. Dušek, J. Fiurášek, and R. Filip, *Physical Review Letters* **107**, 213602 (2011).
- [41] C. Baune, A. Schönbeck, A. Sambrowski, J. Fiurášek, and R. Schnabel, *Optics Express* **22**, 22808 (2014).
- [42] M. Massaro, E. Meyer-Scott, N. Montaut, H. Herrmann, and C. Silberhorn, *New Journal of Physics* **21**, 053038 (2019).
- [43] F. Kaneda, K. Garay-Palmett, A. B. U'Ren, and P. G. Kwiat, *Optics Express* **24**, 10733 (2016).
- [44] S. Signorini and L. Pavesi, *AVS Quantum Science* **2** (2020).
- [45] X.-s. Ma, S. Zotter, J. Kofler, T. Jennewein, and A. Zeilinger, *Physical Review A—Atomic, Molecular, and Optical Physics* **83**, 043814 (2011).
- [46] F. Kaneda, B. G. Christensen, J. J. Wong, H. S. Park, K. T. McCusker, and P. G. Kwiat, *Optica* **2**, 1010 (2015).
- [47] F. Kaneda and P. G. Kwiat, *Science advances* **5**, eaaw8586 (2019).
- [48] S. E. D'Aurelio, M. J. Bayerbach, and S. Barz, *npj Quantum Information* **11**, 37 (2025).
- [49] X. Lu, S. Rogers, T. Gerrits, W. C. Jiang, S. W. Nam, and Q. Lin, *Optica* **3**, 1331 (2016).
- [50] M. G. Genoni, M. L. Palma, T. Tufarelli, S. Olivares, M. S. Kim, and M. G. A. Paris, *Physical Review A* **87**, 062104 (2013).
- [51] I. Straka, A. Predojević, T. Huber, L. Lachman, L. Butschek, M. Miková, M. Mičuda, G. S. Solomon, G. Weihs, M. Ježek, and et al., *Physical Review Letters* **113**, 223603 (2014).
- [52] G. Vidal and R. F. Werner, *Physical Review A* **65**, 032314 (2002).
- [53] M. B. Plenio, *Physical review letters* **95**, 090503 (2005).
- [54] I. Kogias, A. R. Lee, S. Ragy, and G. Adesso, *Physical review letters* **114**, 060403 (2015).
- [55] I. Forbes, F. Ghafari, E. C. Deacon, S. P. Singh, E. Lavie, P. Yard, R. D. Shaw, A. Laing, and N. Tischler, *Reports on Progress in Physics* **88**, 086002 (2025).

ACKNOWLEDGEMENTS

We thank Radmim Filip, Maria Chekhova, Lukáš Lachman and Riccardo Checchinato for helpful comments and discussion. We acknowledge financial support from the European Innovation Council contract EIC open “NanoXCAN” (Grant No. 101047223) (2022-2026) and ”Quantum diffractive Nanoscale Microscopy” (QUINS) and ”Generation of bright non-classical light based on high harmonics and its use in quantum spectroscopy” (GENIOUS) contracts from respectively bilateral (2022-2026) and (2024-2028) ANR-DFG projects (Agence Nationale de la Recherche (ANR) - Deutsche Forschungsgemeinschaft (DFG)). We acknowledge financial support from the CIEDS projects IQUARE (2023-2027) and QUANTIR (2025-2029) and support from the Fondation de l’Ecole Polytechnique under contract X-QUANT (2025-2027). We acknowledge financial support from the department of research of Ecole polytechnique and the X-Innovation Center under contract QUANTIX (2025-2027). H.G. and H.M. acknowledge financial support from the DIM QUANTIP (2024-2027).

AUTHOR CONTRIBUTIONS

D.T. and H.M. conceived the study. D.T., M.N., H.G. and M.W. performed the experiments. D.T. analysed the data. D.T. conducted the numerical analysis with input from I.K. and H.G.. D.T. provided the plots. D.T. wrote the manuscript with input from H.M.. H.M. initiated the quantum HHG research program and acquired the funding. All authors discussed the results.

COMPETING INTERESTS

There are no competing interests to declare.

DATA AND MATERIALS AVAILABILITY

The data and software can be provided after reasonable request to the corresponding author.

SUPPLEMENTARY

Experimental Setup

We employ the setup shown in Fig. S1, generating ultrashort pulses at a central wavelength of $7.7\text{ }\mu\text{m}$ and 100 fs pulses. Two polarizers control the driving laser intensity. An OAP ($f = 100\text{ mm}$) focuses the pulses on the sample (CdTe[110]). In the interaction with the sample, we generate high-order harmonics up to the 15th order spanning a total frequency bandwidth of about 150 THz starting from the 3rd order. A second OAP ($f = 50\text{ mm}$) collimates the emitted radiation, which we then direct through a slightly closed aperture, infrared filter, and a broadband polarizer. The latter is used to dismiss the background luminescence and fluorescence unavoidably generated in the strong-field interaction. Next, we place a flip-mirror in the beam path to direct the radiation towards the spectrometer. The SHHG radiation is then directed towards the setup, which spatially separates three selected HHG orders using dichroic mirrors and spectral filters. We select H11, H12, H13 and H15 in separate measurements. On each harmonic, narrow 10 nm FWHM bandpass filters are placed in front of each detector.

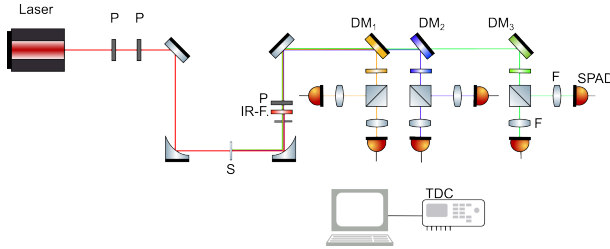


Figure S1. Technical Drawing of the Setup. The driving laser intensity is controlled using a pair of polarizers (P). The driving laser beam is focused onto the sample (S) and the generated high-harmonic emission collimated using off-axis parabolic mirrors. The pump light is filtered using a pinhole and a spectral filter. Luminescence from the sample is suppressed using a broadband polarizer. Three harmonic orders are selected and separated spatially using dichroic mirrors (DM). The single-photon sensitive detectors (SPAD) are arranged in a Hanbury-Brown and Twiss like geometry. Spectral filters with a bandwidth of 10 nm are placed in front of each detector. Single counts and coincidence events are recorded with a time to digital converter.

Calculation of Detection Probabilities

We calculate the non-classicality witness $W_{\text{NC}} = P_{\text{S}} - 2(\sqrt{P_{\text{C}}} - P_{\text{C}})$ from the detection event rates. We evaluate $P_{\text{C}} = \frac{R_{\text{C}}}{N_{\text{P}}}$, where R_{C} the number of coincidence event between two detectors during the measurement duration. N_{P} is the total number of excitation pulses during the same duration. The single event probability is calculated as $P_{\text{S}} = \frac{R_{\text{S,A}} + R_{\text{S,B}} - 2R_{\text{C}}}{N_{\text{P}}}$, where $R_{\text{S,A}}$ and $R_{\text{S,B}}$ the number of single counts on each detector A and B in the detection geometry.

We denote one detector in the scheme Fig. S1 in one spatial mode as the heralding detector. The two-fold coincidence rates $R_{1\text{A}}$ and $R_{1\text{B}}$ are the coincidence rates of one detector in the signal arm and the heralding detector (SA & H, SB & H). The threefold coincidence rate R_2 is a threefold event between the herald detector in mode 2 and both signal detectors (SA & SB & H). R_0 denotes the number of heralding events. With this notation, the vacuum probability is

$$p_0 = 1 - \frac{R_{1\text{A}} + R_{1\text{B}} + R_2}{R_0} \quad (\text{S1})$$

and the estimated single-photon detection probability

$$p_{1,\text{est}} = p_1 = \frac{R_{1\text{A}} + R_{1\text{B}}}{R_0} - \frac{T^2 + (1-T)^2}{2T(1-T)} \frac{R_2}{R_0}, \quad (\text{S2})$$

where T is the effective transmittance of the BS and differences in detection efficiencies [40]. It is implemented as $T_{\text{est}} = R_{1\text{A}}/(R_{1\text{A}} + R_{1\text{B}})$. We note, that the calculation of the heralded ICF with Eq. 3 assumes that higher photon terms are not relevant and we can approximate the conditioned state produced by the source as $\hat{\rho} \approx p_0|0\rangle\langle 0| + p_1|1\rangle\langle 1| + (1-p_0-p_1)|2\rangle\langle 2|$. Thus, we limit our experiment to a low number of mean photons.

We also confirmed that exactly the same heralded $g^{(2)}$ values are obtained, when directly calculated from the count rates instead of the probabilities via

$$g_{\text{h}}^{(2)} = \frac{R_2 \cdot R_0}{R_{1\text{A}} R_{1\text{B}}} \quad (\text{S3})$$

as described, e.g. in [42–44]. This additionally confirms that the state is well approximated by the density matrix above and that multi-photon errors are negligible.

Effective State Model

We can evaluate another useful metric, the quantum non-Gaussian depth (QNGD) of the heralded single-photon state. The QNGD is defined as

$$T_{\text{SPS}} = -10 \log(T_{\text{min}}) = -10 \log \left(\frac{3}{2} \frac{p_{2+}}{p_1^3} \right) \text{ dB} \quad (\text{S4})$$

and given in dB [51]. Intuitively, it quantifies the amount of attenuation the state can withstand before losing its QNG property. It is an approachable operative metric that is more robust than the detection of Wigner negativity.

The full two-mode generalized Gaussian density matrix is

$$\hat{\rho}_{\text{out}} = \hat{D} \hat{U}_{\text{BS2}} \hat{S} \hat{U}_{\text{BS1}} \hat{\rho}_{\text{in}} \hat{U}_{\text{BS1}}^\dagger \hat{S}^\dagger \hat{U}_{\text{BS2}}^\dagger \hat{D}^\dagger, \quad (\text{S5})$$

where $\hat{\rho}_{\text{in}} = \hat{\rho}_{\text{th},1} \otimes \hat{\rho}_{\text{th},2}$, $\hat{D} = \hat{D}_1(\alpha_1) \otimes \hat{D}_2(\alpha_2)$ and $\hat{S} = \hat{S}_1(\zeta_1) \otimes \hat{S}_2(\zeta_2)$.

Two thermal states are initialized as a product state $\hat{\rho}_{\text{th},1} \otimes \hat{\rho}_{\text{th},2}$ parametrized by the thermal occupation numbers $n_{\text{th},1}$ and $n_{\text{th},2}$. These two states are mixed on

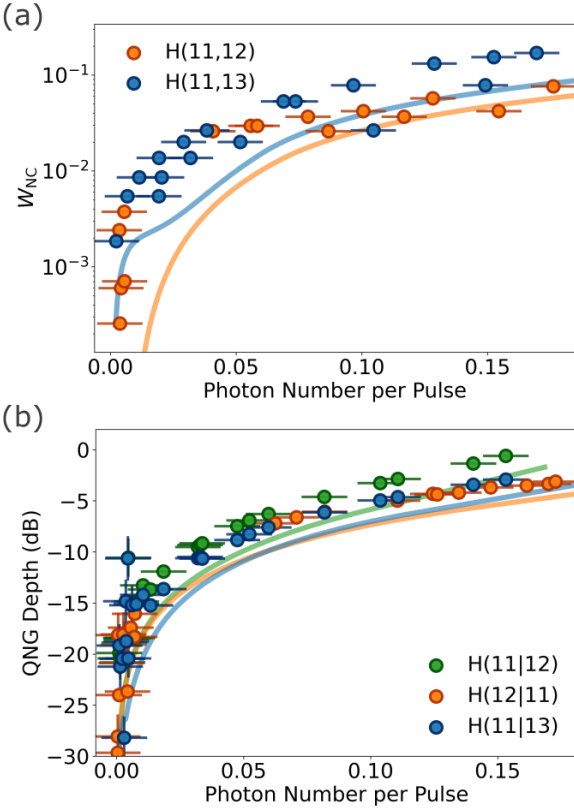


Figure S2. Additional non-classical Criteria. We show the non-classicality witness introduced in the main text, evaluated for the cross-correlation between two distinct harmonic orders. Figure (b) shows the quantum non-Gaussian depth (QNGD), an additional metric for the quantum non-Gaussian nature of the heralded state. Intuitively it measures how much attenuation the state can withstand, before losing its QNG character. Although our measurement only approaches the critical bound of 0, we still employ the trend as a useful metric for the optimization.

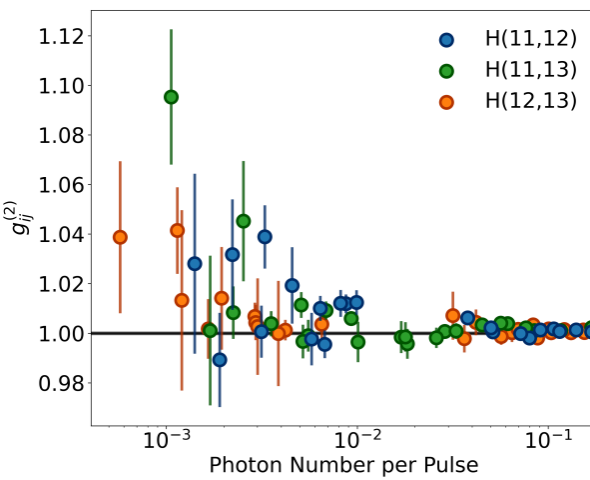


Figure S3. Cross Intensity Correlation Function. Measured normalized intensity correlation function $g_{H(i,j)}^{(2)}$ calculated from single- and coincidence events between two harmonic orders ($i \neq j$).

a beamsplitter (BS_1) modelled by a unitary transformation $\hat{U}_{BS}(\theta, \phi) = \exp[\theta(e^{-i\phi}\hat{a}_1\hat{a}_2^\dagger - e^{i\phi}\hat{a}_1^\dagger\hat{a}_2)]$, where θ is the mixing angle related to the transmission $|T| = \cos \theta$ and reflection $|R| = \sin \theta$ and ϕ_{BS} is a phase shift between the reflected and transmitted path. After the first beamsplitter mixing, single mode squeezing is applied to each mode independently. This is achieved by applying the unitary squeezing operator $\hat{S}(\xi)$ with $\xi = r \exp i\phi_{sq}$, to each mode. Next, a second beamsplitter operation $\hat{U}_{BS2}(\theta, \phi_{BS2})$ is performed. Finally, each mode is displaced with the displacement operators $\hat{D}_1(\alpha_1)$ and $\hat{D}_2(\alpha_2)$.

One main aspect of the model is that we parametrize some variables with a change in the driving laser intensity I . As the driving laser intensity fluctuates during the measurement, rendering the initial characterization inaccurate for the hour long measurements, we parametrize the intensity by an independent variable I . It is central in modelling the scaling of the state with the driving intensity. The scaling dependencies are simple power laws and are given for harmonic mode k as

$$n_{th,k}(I) = s_{th,k} I^{\beta_{th,k}} \quad (S6)$$

$$r_k(I) = s_{r_k} I^{\beta_{r_k}} \quad (S7)$$

$$|\alpha_k(I)| = s_{\alpha_k} I^{\beta_{\alpha_k}/2} \quad (S8)$$

for the thermal photon number, the squeezing parameter and the displacement amplitude. The factors s are scaling factors and β are the power-law exponents. The model's aim is to describe the scaling of the quantum states properties over a common variable, the driving laser intensity.

In total, including the parameters for the unitary transformations, the model incorporates 17 free parameters. The use of this parameter space without overfitting is justified by the large volume of experimental data across five distinct observables. The optimization is performed simultaneously to these observables, namely the heralded intensity correlation function $g_h^{(2)}$, the non-classicality witness for both individual harmonics and their cross-correlation, and the quantum non-Gaussian depth.

The normalized root-mean-square error (NRMSE) of the model's quantum statistics and the experimental data is calculated across all observables. To achieve a good fit, the errors are weighted by relative importance. The weighting scheme is chosen to prioritize the model's ability to reproduce the key non-classical features of the state. The start and endpoints receive high importance, and an additional penalty is applied when the overall range exceeds largely the experimental data.

Finding a convergent solution is challenging because of the large parameter space. We start a multi-stage optimization with a global search. Initially, the parameter space is restricted with a random search and refined via differential evolution. This initial restriction is necessary to avoid being trapped in a local minimum early on, while exploring the large parameter space for promising solutions. Subsequently, we run a local algorithm for refinement of the initial global solution. We use the

dual annealing algorithm, which is especially designed for the optimization of multidimensional functions. During the optimization process, it became apparent that the solutions were insensitive to the beamsplitter phase ϕ_{BS1} , which consistently converged to near-zero values. Furthermore, the optimal fits corresponded to amplitude

squeezing. Therefore, to increase the stability and physical clarity of the model, we fixed the squeezing angles $\phi_{sq} = \pi$ to focus on amplitude squeezing and set the beamsplitter phase ϕ_{BS1} to zero, reducing the final number of free parameters to 16. The optimized parameters are reported in Table S1.

Parameter	Description	H(11 13)	H(11 12)	H(12 11)	Mean \pm Std
I_0	Intensity factor	234.91	230.00	231.65	232.2 ± 2.5
$n_{\text{th},s}^{(0)}$	Thermal scale (signal)	3.2×10^{-3}	7.6×10^{-5}	1.0×10^{-5}	—
$\beta_{n_{\text{th},s}}^{(0)}$	Thermal exponent (signal)	0.52	0.56	0.52	0.53 ± 0.02
$n_{\text{th},h}^{(0)}$	Thermal scale (herald)	6.7×10^{-3}	1.0×10^{-5}	1.0×10^{-5}	—
$\beta_{n_{\text{th},h}}^{(0)}$	Thermal exponent (herald)	0.12	0.60	0.54	0.42 ± 0.26
$r_s^{(0)}$	Squeezing scale (signal)	0.095	0.145	0.071	0.10 ± 0.04
$\beta_{r_s}^{(0)}$	Squeezing exponent (signal)	1.18	1.29	1.18	1.22 ± 0.07
$r_h^{(0)}$	Squeezing scale (herald)	0.573	0.556	0.571	0.567 ± 0.009
$\beta_{r_h}^{(0)}$	Squeezing exponent (herald)	1.60	1.79	1.75	1.71 ± 0.10
ϕ_s	Squeezing phase (signal)	3.150	3.142	3.132	3.141 ± 0.009
ϕ_h	Squeezing phase (herald)	3.142	3.144	3.132	3.139 ± 0.007
$\alpha_s^{(0)}$	Displacement scale (signal)	0.881	0.711	0.864	0.82 ± 0.09
$\beta_{\alpha_s}^{(0)}$	Displacement exponent (signal)	2.52	2.16	2.21	2.30 ± 0.19
$\alpha_h^{(0)}$	Displacement scale (herald)	0.433	0.384	0.482	0.43 ± 0.05
$\beta_{\alpha_h}^{(0)}$	Displacement exponent (herald)	1.57	1.67	1.64	1.63 ± 0.05
$\theta_{\text{BS},1}$	Beamsplitter 1 angle	0.410	0.486	0.509	0.47 ± 0.05
$\phi_{\text{BS},1}$	Beamsplitter 1 phase	0.021	0.006	0.021	≈ 0
$\theta_{\text{BS},2}$	Beamsplitter 2 angle	1.399	1.673	1.558	1.54 ± 0.14
$\phi_{\text{BS},2}$	Beamsplitter 2 phase	-1.29	-1.68	-1.48	-1.48 ± 0.20

Table S1. Optimized model parameters for each harmonic combination. All intensity scaling exponents β are reported such that the corresponding quantity scales as I^β . Phases are reported in radians.